processes

MDPI

Article

Composite Anion Exchange Membranes Based on Functionalized Graphene Oxide and Poly(Terphenylene Piperidinium) for Application in Water Electrolysis and Fuel Cells

Tamilazhagan Palanivel [1,*], Hosni Ahmed Elwan [2], Mohamed Mamlouk [2], Simon Doherty [3] and Bruno G. Pollet [1,*]

[1] Clean Hydrogen Lab, Hydrogen Research Institute (HRI), Université du Québec à Trois-Rivières (UQTR), 3351 Boulevard des Forges, Trois-Rivières, QC G9A 5H7, Canada
[2] School of Engineering, Merz Court, Newcastle University, Newcastle upon Tyne NE1 7RU, UK; hosni-ahmed.elwan-atout@newcastle.ac.uk (H.A.E.); mohamed.mamlouk@newcastle.ac.uk (M.M.)
[3] School of Natural and Environmental Sciences, Chemistry, Bedson Building, Newcastle University, Newcastle upon Tyne NE1 7RU, UK; simon.doherty@newcastle.ac.uk
* Correspondence: tamilazhagan.palanivel@uqtr.ca (T.P.); bruno.pollet@uqtr.ca (B.G.P.)

Abstract

Composite anion exchange membranes (AEMs) based on poly(terphenylene piperidinium) (PTPiQA) and impregnated with varying loadings of quaternized graphene oxide (QGO) as filler were developed, and their properties as anion exchange membranes for use in water electrolysis (AEMWEs) and fuel cells (AEMFCs) were explored. This study investigates the trade-off between mechanical robustness, ionic conductivity, and alkaline stability in QGO-reinforced twisted polymer backbones. QGO synthesized by functionalization with ethylenediamine (EDA), followed by quaternization with glycidyl trimethylammonium chloride (GTMAC), was used as a filler for PTPiQA, and the properties of the resulting composites PTPiQA-QGO-X investigated as a function of QGO loading for X between 0.1 and 0.7 wt%. Among all compositions, PTPiQA-QGO-0.3% exhibited the highest OH^- conductivity of 71.56 mS cm^{-1} at room temperature, attributed to enhanced ionic connectivity and water uptake. However, this increase in conductivity was accompanied by a slight decrease in ion exchange capacity (IEC) retention (91.8%) during an alkaline stability test in 1 M KOH at 60 °C for 336 h due to localized cation degradation. Mechanical testing revealed that PTPiQA-QGO-0.3% offered optimal dry and wet tensile strength (dry TS of 42.77 MPa and wet TS of 30.20 MPa), whereas higher QGO loadings yielded low mechanical strength. These findings highlight that 0.3 wt% QGO balances ion transport efficiency and mechanical strength, while higher loadings improve alkaline durability, compromising mechanical durability and guiding the rational design of AEMs for AEMWEs and AEMFCs.

Keywords: polymer composites; anion exchange membrane; hydrogen; water electrolysis; fuel cells; functionalized graphene oxide; poly(terphenylene piperidinium); mechanical stability; ionic conductivity

check for updates

Academic Editors: Md Nizam Uddin and Faycal Znidi

Received: 17 May 2025
Revised: 14 September 2025
Accepted: 19 September 2025
Published: 24 September 2025

Citation: Palanivel, T.; Elwan, H.A.; Mamlouk, M.; Doherty, S.; Pollet, B.G. Composite Anion Exchange Membranes Based on Functionalized Graphene Oxide and Poly (Terphenylene Piperidinium) for Application in Water Electrolysis and Fuel Cells. *Processes* **2025**, *13*, 3047. https://doi.org/10.3390/pr13103047

Copyright: © 2025 by the authors. Licensee MDPI, Basel, Switzerland. This article is an open access article distributed under the terms and conditions of the Creative Commons Attribution (CC BY) license (https://creativecommons.org/licenses/by/4.0/).

1. Introduction

The escalating global demand for energy, driven by technological progress and industrial growth, necessitates the development of sustainable and efficient energy sources [1,2]. At present, fossil fuels continue to dominate the global energy landscape, but their extensive exploitation poses significant environmental challenges and continues to deplete these

dwindling natural resources [3,4]. Consequently, there is an urgent need to develop clean and renewable energy technologies capable of meeting future energy requirements while reducing carbon emissions [5]. Among various emerging alternatives, anion exchange membrane water electrolysers (AEMWE) [6] and fuel cells (AEMFC) [7] shown in Figure 1a,b, respectively, have gained considerable attention due to their high efficiency and minimal environmental impact. AEMFCs, in particular, are emerging as a promising candidate due to their enhanced oxygen reduction kinetics [8] and the feasibility of utilizing nonprecious metal catalysts [9], significantly reducing costs compared to proton exchange membrane fuel cells (PEMFCs) [10] and other types such as solid oxide fuel cells (SOFCs) [11].

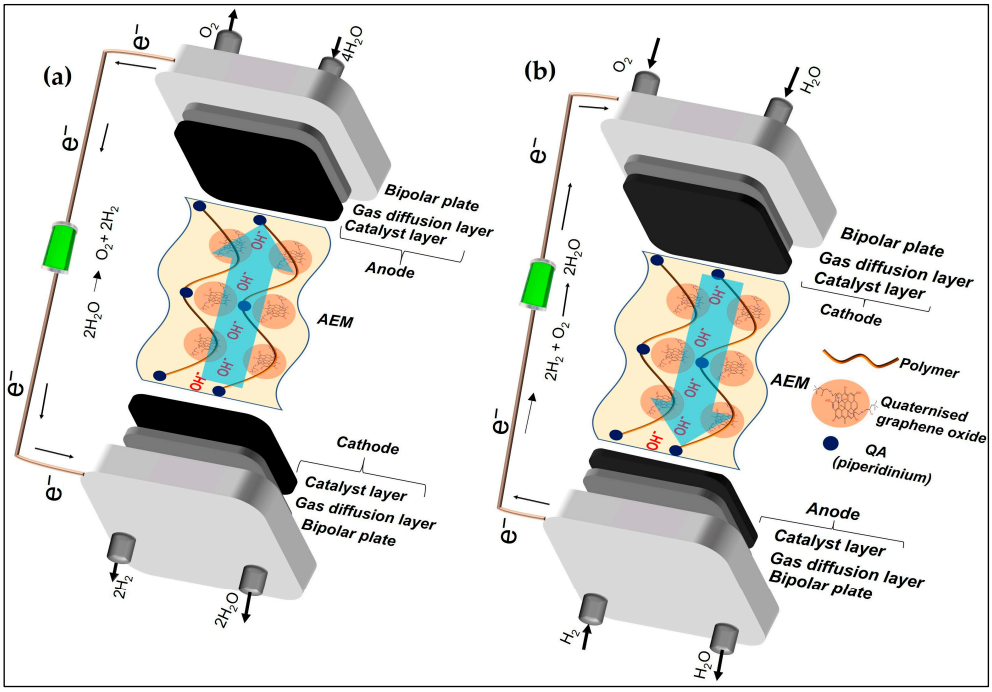


Figure 1. Schematic illustration of (**a**) AEMWE, (**b**) AEMFC.

Despite their potential, conventional AEMs still face several critical challenges, including limited alkaline stability, inadequate ionic conductivity, and insufficient dimensional control under hydrated conditions [12]. In addition to these material limitations, one of the most pressing challenges for AEMFCs is their limited operational durability and lifespan. During prolonged operation, performance degradation often occurs due to the complex electrochemical environment and component aging, ultimately hindering commercial viability [13]. Additionally, achieving high power densities in AEMFCs requires effective water management, as excess water at high current densities can lead to flooding and hinder gas diffusion, ultimately reducing fuel cell durability [14]. These shortcomings are largely attributed to the chemical vulnerability of the anion exchange membrane [15] in the alkaline environment of the fuel cell, where degradation occurs through Hoffmann elimination or nucleophilic dealkylative substitution [16], which ultimately compromises membrane durability and longevity [17]. To overcome these issues, researchers have focused on enhancing the durability of AEMs by incorporating various cationic groups, including imidazolium [18], pyrrolidinium [19], phosphonium [20], and spirocyclic [21] and heterocyclic QA moieties [22]. In addition, incorporation of a filler into the anion exchange polyelectrolyte has been shown to improve mechanical and chemical stability. To this end, graphene oxide (GO) has attracted significant interest due to its unique two-dimensional structure, high surface area, and ability to be chemically functionalized to enhance compatibility with the polymer matrix [23]. However, the inherent drawbacks of GO, including

its tendency to aggregate [24] and its insufficient mechanical stability, necessitate further chemical modification to enhance its integration and performance in AEMs.

Quaternized GO (QGO) has emerged as a promising modification of GO to address these challenges [25], as the introduction of QA groups onto the GO surface provides additional ion exchange sites, which enhance the overall ionic conductivity of the membrane [26]. Various studies have demonstrated that incorporating QGO into polymer backbones can significantly increase the IEC and water uptake (WU) through the formation of interconnected ionic clusters, while also maintaining dimensional stability through robust polymer–filler interactions. For example, incorporating QGO as a filler into quaternized cellulose/polyphenylene oxide (PPO)-crosslinked AEMs has been shown to enhance ionic conductivity, although it results in a reduced IEC [27]. Similarly, integrating reduced quaternized GO into quaternized polyphenylene oxide (QPPO) improved AEMFC performance [28], while amine-functionalized GO and QPPO composites enhanced ionic conductivity [29]. More recently, the incorporation of QGO, prepared by GO functionalization with 4,4′-methylenedianiline (MDA) and subsequent quaternization with glycidyltrimethylammonium chloride (GTMAC) into QPPO was reported to improve ionic conductivity, thermal stability, and mechanical strength [30].

In this study, twisted poly(terphenylene piperidinium)-based nanocomposite AEMs have been developed by incorporating QGO as a functional nanofiller on the basis that the combination of the twisted polymer backbone and the QGO will enhance rigidity and dimensional stability, while free volume will facilitate the formation of microphase-separated domains and thereby enhance ion transport. To this end, the formation of microphase-separated morphologies enhances anion transport and conductivity by creating continuous hydrated channels [31]. In AEMs, phase separation between hydrophilic (cationic) and hydrophobic (structural) domains reduces tortuosity and facilitates directional hydroxide transport, avoiding the limitations of randomly distributed ionic sites [32–34]. Rather than forming isolated pockets, the hydrophilic regions aggregate into percolated networks during hydration. These networks form continuous, hydrated ion-conducting channels across the membrane driven by hydration-induced swelling of the cationic regions (Figure S4) [35–38].

The twisted geometry of the poly(terphenylene piperidinium) backbone introduces free volume that enables better spatial rearrangement of hydrophilic segments, which enhances their clustering and continuity. Together, these effects yield nanostructured morphologies where hydrophilic regions are not disrupted by the surrounding hydrophobic matrix, but are rather interconnected to enable efficient hydroxide ion transport. In this study, the impact of QGO filler on the membrane properties was investigated by systematically varying the QGO content (0.1%, 0.3%, 0.5%, and 0.7% by weight). Notably, incorporation of 0.3 wt% QGO resulted in a significant improvement in the mechanical stability and ionic conductivity of the membrane, and, although the use of 0.5–0.7 wt% QGO gave the highest stability, the composites lacked mechanical integrity. This study provides valuable insights into the design of high-performance AEMs through the strategic incorporation of QGO, and underlines the potential of these nanocomposites as membranes for applications in fuel cells and electrolysers.

2. Materials and Methods

2.1. Chemicals and Materials

m-Terphenyl(99%)-T3009, 4-piperidone monohydrate hydrochloride(PMH-98%)-151769, trifluoromethanesulfonic acid (TFSA)-8.21166, *N*,*N*-diisopropylethylamine(DIPEA > 99%)-D125806, sodium chloride-S9888, and silver nitrate ($AgNO_3$)-1.11718, glycidyl trimethylammonium chloride (GTMAC)-50053, were purchased from Sigma-Aldrich (Oakville, ON, Canada). Dichloromethane (DCM)-MDX08346, sodium sulfate (Na_2SO_4)-S421, ethyl alcohol (EtOH)-

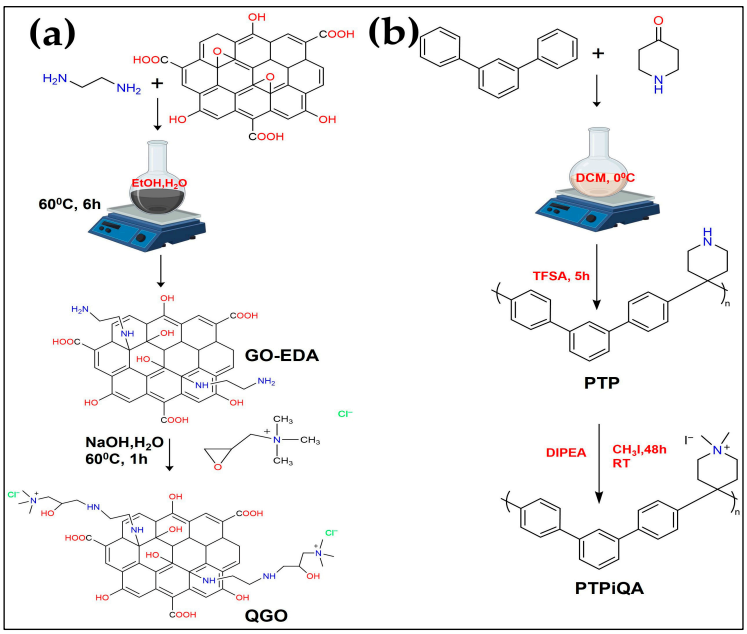
LC222004, and ethylenediamine (EDA-98.0+%)-E0077500ML were purchased from Fisher Scientific (Ottawa, ON, Canada). Iodomethane (CH_3I)-AC122371000, potassium chromate (K_2CrO_4)-AA1261022, and potassium hydroxide-P251 were purchased from Fisher Scientific (Ottawa, ON, Canada). Graphene oxide was purchased from Standard Graphene (Ulsan, Republic of Korea). Dimethyl sulfoxide(DMSO)-B0CJMMBT3P was purchased from GARCHEM (Kąkolewo, Poland). All the chemicals and reagents are of analytical grade and were used as received.

2.2. Methods and Characterization

2.2.1. Synthesis Methods

- Functionalization of graphene oxide

QGO was synthesized following a previously reported procedure, as shown in Scheme 1a [30]. Briefly, GO (1.0 g) was dispersed in a solvent comprising 50 mL of ethanol and 30 mL of double-distilled water (DDW) and sonicated for 1 h to achieve a homogeneous dispersion. EDA (0.36 g) was then added, and the resulting mixture was heated at 60 °C for 6 h. After this time, the mixture was allowed to cool to room temperature, filtered, and the resulting solid washed thoroughly with ethanol and DDW to remove any unreacted amine, and the GO-EDA dried at 60 °C for 24 h. For the quaternization, GO–EDA (0.200 g) was redispersed in deionized water (30 mL) containing GTMAC (0.190 mL) and NaOH (0.06 g). The mixture was stirred at 60 °C for 1 h and then left at room temperature for a further 24 h. The QGO was collected by filtration, washed thoroughly with ethanol and water, and dried under vacuum.



Scheme 1. (**a**) Synthesis of surface-functionalized QGO; (**b**) Synthesis of poly(terphenylene piperidine) and poly(terphenylene piperidinium) iodide with piperidinium groups.

- Synthesis of Poly(terphenylene piperidinium)

Synthesis of poly(terphenylene piperidinium) (PTPiQA) iodide was carried out via Friedel–Crafts polycondensation, following a previously reported procedure (Scheme 1b) [39]. A 250 mL round-bottom flask equipped with a magnetic stir bar was charged with *m*-terphenyl (2.30 g), 4-piperidone monohydrate hydrochloride (1.49 g), and dichloromethane (50 mL) and stirred to obtain a homogeneous solution. The mixture was then cooled to 0 °C, and trifluoromethanesulfonic acid (8.8 mL) was added dropwise, leading to a color change from

purple to black. The reaction was stirred for 5 h, during which time the viscosity increased quite significantly. The resulting highly viscous black solution was then slowly poured into DI water, leading to the formation of a large amount of precipitate, which was isolated by filtration, washed with DI water to remove residual reactants, and dried at room temperature for 24 h to afford poly(terphenylene piperidine) (PTP) as a light-yellow powder. PTP (0.20 g) was dissolved in DMSO (5 mL), DIPEA (0.01 mL) was added, and the resulting homogeneous solution was cast onto a Petri dish and allowed to stand at room temperature for 12 h, after which it was transferred to an oven and dried at 80 °C for 24 h. The resulting film was immersed in an iodomethane solution (0.15 mL in 5 mL MeOH) and kept in the dark at room temperature for 24 h. The quaternized membrane was washed thoroughly with deionized water to remove unreacted iodomethane and then immersed in aqueous 1 M KOH at room temperature for 48 h to exchange the iodide for hydroxide. The membranes were then thoroughly washed with deionized water and dried at 60 °C for 24 h.

- Fabrication of PTPiQA-QGO-X membranes

The PTPiQA-QGO-X membranes were fabricated using a solution casting method. First, PTP (0.30 g) was dissolved in DMSO (3.0 mL) under constant stirring at room temperature for 2 h to ensure complete dissolution, after which DIPEA (0.01 mL) was added. Simultaneously, QGO at different concentrations (0.1 to 0.7 wt%) was dispersed in 2 mL of DMSO by ultrasonication for 2 h to achieve a stable dispersion. The QGO dispersion was then slowly added to the deprotonated PTP solution, and the mixture was sonicated for a further 2 h to obtain a homogeneous blend, as shown in Figure 2. The resulting solution was cast onto a clean glass Petri dish and kept at room temperature for 12 h, after which it was dried in a vacuum oven at 60 °C for 48 h to remove residual solvent. After drying, the membranes were carefully peeled off and immersed in excess iodomethane (2 mL) in a sealed container and left to stand at room temperature for 24 h. After this time, the membrane was removed, washed with DI water, and then immersed in aqueous 1 M KOH for 48 h to obtain the hydroxide form. The membranes were then thoroughly washed with deionized water and dried at 60 °C under vacuum for 24 h. The final membranes had a thickness in the range of 57–145 µm and were designated as PTPiQA for the neat membrane and PTPiQA-QGO-X, where X denotes the weight percentage (0.1 to 0.7 wt%) of QGO into the polymer matrix.

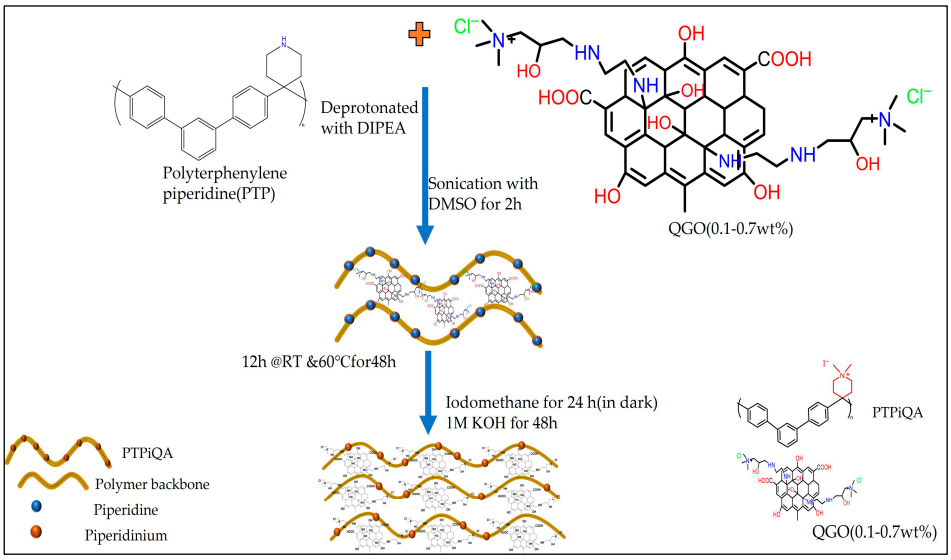


Figure 2. Fabrication of PTPiQA-QGO-X composite membranes.

2.2.2. Characterization

- Morphology, composition, and mechanical and thermal stability

Raman spectroscopy was performed using a Raman Touch microscope with Nano photon (Osaka, Japan) to investigate the degree of structural disorder in GO and its quaternized form. The composition of *m*-TPN, PTP, and PTPiQA was confirmed by ^{1}H nuclear magnetic resonance (NMR) spectroscopy using a Bruker DRX-400 instrument (Karlsruhe, Germany). Functional group analysis of GO, and confirmation of its chemical modifications through functionalization and quaternization, was obtained using Fourier-transform infrared (FTIR) spectroscopy, Nicolet Impact 400, Thermo Scientific (Waltham, MA, USA) with a ZnSe crystal, covering the range of 4000 to 500 cm^{-1}. FTIR spectroscopy was also applied to study the PTPiQA and PTPiQA-QGO-X membranes. An Agilent Cary 60 UV–Vis spectrophotometer (Santa Clara, CA, USA), was used to record the transmission spectra of the membranes in the wavelength range of 200–800 nm.

The morphology of GO and QGO, along with the surface and cross-sectional structures of PTPiQA and PTPiQA-QGO-X membranes, was explored using scanning electron microscopy (SEM), utilizing the Hitachi SU1510 VP SEM (Tokyo, Japan), operated at an acceleration voltage of 20 keV. X-ray photoelectron spectra were obtained using a PHI Quantes spectrometer equipped with a monochromatic Al Kα X-ray source (hν = 1486.6 eV) (Chigasaki, Japan). Atomic force microscopy (AFM), Asylum Research MFP-3D™ (Santa Barbara, CA, USA) was used to analyze the membrane topography and to measure the membrane roughness. The parameters for the surface roughness were represented by the mean difference between the highest peaks and the lowest valleys (Sz), the Z data's root mean square (Sq), and the average roughness (Sa). Thermal properties of PTPiQA-QGO-X membranes were evaluated using a Perkin-Elmer Pyris-1 analyzer (Waltham, MA, USA), from 30 °C to 650 °C at a heating rate of 10 °C/min under an oxygen atmosphere. Mechanical performance of the membranes was tested in wet and dry conditions using a universal testing machine, Instron (Norwood, MA, USA) at a constant crosshead speed of 10 mm/min to determine their tensile strength (TS) and elongation at break (EB).

- Ion exchange capacity

The IEC was measured by Mohr's method. In a typical procedure, the membrane was immersed in an aqueous solution of NaCl (1 mol L^{-1}) for 24 h, then washed with DI water to remove the absorbed NaCl and dried to a constant weight. The fully dried membrane was weighed, and the weight was denoted as W_{dry}. Finally, the membrane was soaked in aqueous Na_2SO_4 (0.5 mol L^{-1}) for 24 h to exchange the Cl^- for $SO_4{}^{2-}$. The Cl^- released from the membrane was then titrated with 0.05 M aqueous $AgNO_3$ using K_2CrO_4 as the colorimetric indicator. The IEC was then calculated from the amount of $AgNO_3$ consumed during titration and the mass of the dry membrane in Cl^- form (W_{dry}) according to Equation (1):

$$\mathrm{IEC(mmol/g)} = V(\mathrm{AgNO_3}) \times C(\mathrm{AgNO_3})/W_{dry} \quad (1)$$

- Water uptake and linear swelling ratio

Membrane samples were immersed in distilled water at room temperature for 24 h, then removed, and the membrane surface was quickly wiped with tissue paper. Water uptake and the linear swelling ratio (LSR) of the membranes were calculated from the mass and length of wet and dry samples using Equations (2) and (3):

$$\mathrm{WU(\%)} = W_{we}t - W_{dry}/W_{dry} \times 100\% \quad (2)$$

$$\mathrm{LSR(\%)} = L_{wet} - L_{dry}/L_{dry} \times 100\% \quad (3)$$

where W_{wet} and L_{wet} are the weight and length of the wet membrane, and W_{dry} and L_{dry} are those of the membrane after drying at 60 °C in a vacuum oven for 24 h, respectively.

- Hydroxide conductivity

The in-plane ionic conductivity of the membranes was evaluated using a two-probe setup with DI water circulation at room temperature. Prior to measurement, membranes were converted to the hydroxide form by immersing them in aqueous 1 M KOH, with the solution replaced every 20 min over a period of 1 h. The conductivity cell consisted of two parallel platinum electrodes fixed at a distance of d = 0.5 cm apart. The membrane sample was set onto the electrodes, ensuring good contact (Figure 3). Electrochemical impedance spectroscopy (EIS) was performed at room temperature, and the membrane resistance (R) was obtained from the high-frequency intercept of the Nyquist plot. The in-plane ionic conductivity (σ) was calculated using Equation (4):

$$\sigma = \frac{d}{W \times T \times R} \quad (4)$$

where σ is the in-plane conductivity (mS cm^{-1}), d is the electrode gap (0.5 cm), W is the width of the membrane (cm), T is the membrane thickness (cm), and R is the measured resistance (Ω).

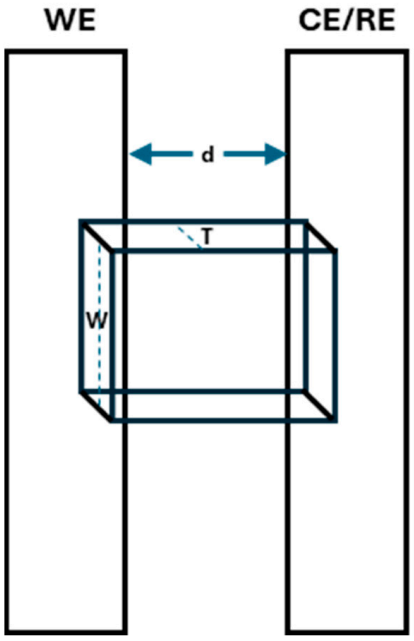


Figure 3. In-plane ionic conductivity setup.

- Alkaline stability

The membrane with a size of 1 cm × 1 cm was placed in aqueous 1 M KOH at 60 °C for 336 h. The IEC of AEM was measured before and after to estimate its alkaline stability.

3. Results and Discussion

3.1. Structural and Morphological Characterizations of GO and QGO

In this study, the Raman spectrum of pristine GO in Figure 4a contains two key bands, the D band at 1343.80 cm^{-1} and the G band at 1591.24 cm^{-1}. The D band is linked to structural defects and disruptions in the graphene lattice, while the G band represents the in-plane vibrational modes of sp^2 carbon atoms, which form the backbone of the graphene lattice [40]. The intensity ratio of these peaks (I_D/I_G) was 0.97, indicating a moderate level of disorder in

pristine GO. After functionalization, the spectrum of QGO showed slight shifts in these bands, with the D band appearing at 1343.74 cm^{-1} and the G band at 1582.66 cm^{-1}.

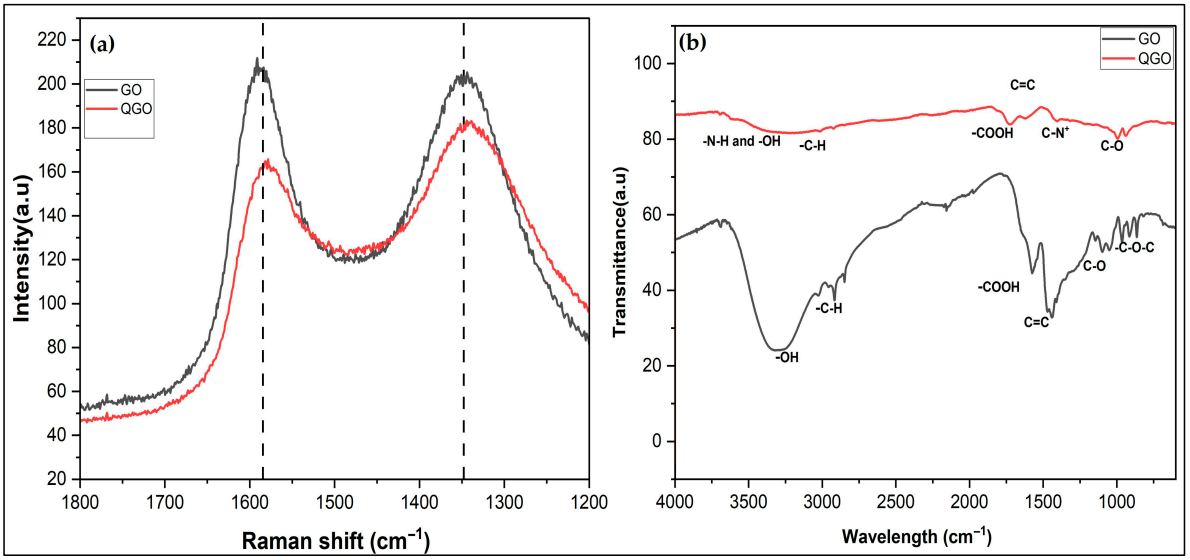


Figure 4. (**a**) Raman spectra of GO and QGO; (**b**) FT-IR spectra of GO and QGO.

These shifts suggest that structural changes occurred as a result of the attachment of the QA groups. Furthermore, the (I_D/I_G) ratio increased to 1.08, indicating that more structural defects were introduced during the chemical functionalization. Overall, these changes in the Raman spectrum provide evidence for the successful functionalization of GO to afford QGO. The increase in the (I_D/I_G) ratio aligns with previous findings on chemically modified graphene [30], where functionalization typically introduces new structural defects while retaining the fundamental sp^2 carbon network. Further, the FT-IR spectra of GO and QGO in Figure 4b display distinct differences, confirming the successful quaternization of graphene oxide. In the GO spectrum, characteristic peaks are at 3400 cm^{-1} (-OH stretching), 2920 cm^{-1} (-C-H stretching), 1720 cm^{-1} (-COOH stretching), and 1500–1000 cm^{-1} (C=C, C-O-C, and C-O stretching), indicate the presence of hydroxyl, carbonyl, conjugated C=C, and epoxy groups typical of graphene oxide. Upon quaternization, the QGO spectrum exhibits a significant decrease in the intensity of oxygen-containing bands, especially those associated with -OH and -COOH, indicating partial reduction or modification of these functional groups. Notably, a distinct C-N^+ stretching band at 1459 cm^{-1} strongly indicates the presence of quaternary ammonium groups, confirming successful quaternization of GO [27], while the broad band at 3200 cm^{-1} is associated with the N-H of the ethylenediamine. To further validate the quaternization, surface characterization was undertaken by X-ray photoelectron spectroscopy. The N 1 s region of QGO (Figure S1a) displayed two distinct bands at 402.66 eV and 399.56 eV, corresponding to quaternary nitrogen and residual amine, respectively, thereby confirming the successful quaternization of QGO [27].

3.2. Structural and Morphological Characterizations of Polymer

The ^1H NMR spectra in Figure 5a–c highlight the structural differences between the terphenyl monomer, poly(terphenylene piperidine), and poly(terphenylene piperidinium) iodide.

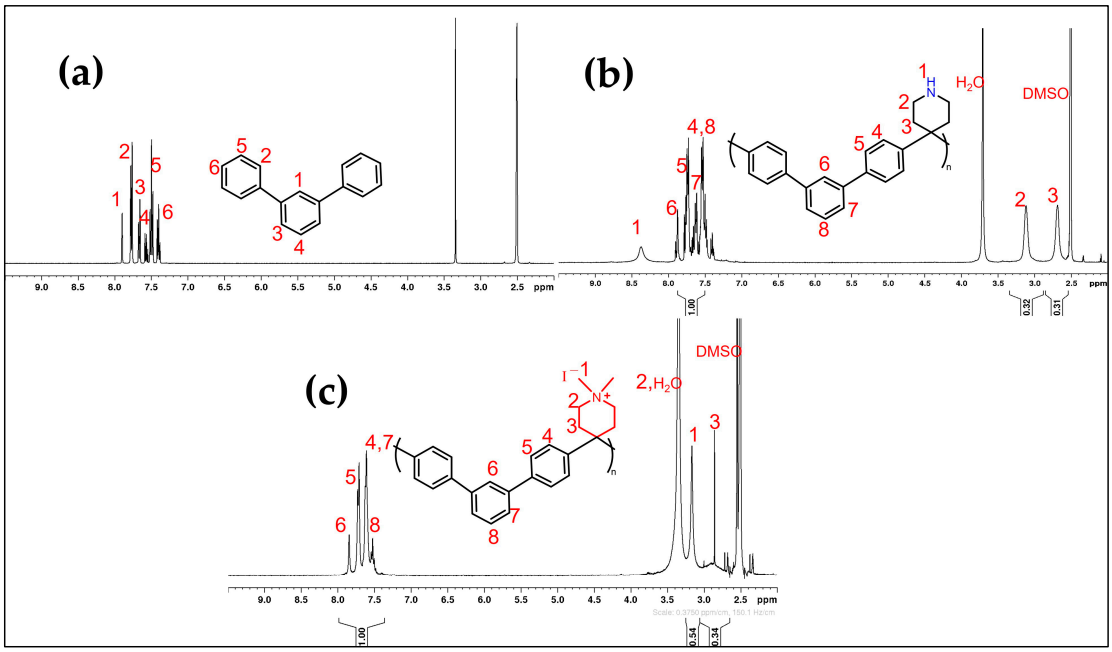


Figure 5. ^{1}H NMR spectra of (**a**) *m*-TPN, (**b**) PTP, and (**c**) PTPiQA.

The aromatic protons of the terphenylene backbone (H1–H6) appeared as a series of multiplets in the expected region between δ 7.0 and 8.0 ppm (Figure 5a). After co-polymerization with piperidine, the resulting polymer contained new signals, δ 3.2 ppm and δ 2.6 ppm, associated with methylene protons H2 and H3, respectively, of the piperidine ring and an N-H proton (H1) at 8.4 ppm (Figure 5b). The integration ratio of the aromatic region (H4–H8) to the methylene protons (H2) was determined to be 3:1, which aligns with the previous report [39]. Quaternization of the polymer with methyl iodide led to the complete disappearance of the N–H signal at δ 8.4 ppm, indicating complete conversion to the quaternary ammonium polymer (Figure 5c). In addition, new peaks at δ 2.9 ppm and δ 3.2 ppm belong to the *N*-methyl protons (H1) and the methylene (H2) protons adjacent to the quaternized nitrogen. The aromatic signals remained largely unchanged, confirming the structural integrity of the backbone. These observations are consistent with previous findings and confirm the successful synthesis [39]. Additionally, the N 1s region of the XPS spectrum of PTPiQA (Figure S1b), contains characteristic peaks at 401.85 eV, attributed to quaternary nitrogen [41] and 399.85 eV assigned to a minor amount of residual piperidine nitrogen. These results verify the effective quaternization of PTPiQA.

3.3. Structural Characterizations of PTPiQA and PTPiQA-QGO-X Membranes

3.3.1. FT-IR

The FT-IR spectra of PTPiQA and PTPiQA-QGO-X (X = 0.1–0.7 wt%) in Figure 6a display characteristic broad bands around 3500 cm^{-1} attributed to the stretching vibrations of hydroxyl (-OH) groups; these primarily arise from absorbed water and residual hydroxyl functionalities within the QGO. The intensity of this broad band increases as the QGO content rises, indicating that the introduction of QGO enhances the hydrophilicity of the membrane [42]. Additionally, the aromatic framework of the polymer is evident from the band around 1600 cm^{-1} corresponding to the stretching vibrations of the aromatic C=C bonds within the polyterphenylene backbone and the QGO. A minor band around 1459 cm^{-1} is assigned to the C–N^+ stretching mode in the QGO [27], and the characteristic C–N stretching vibration at 1220 cm^{-1} remains visible in the composite membranes, and a distinct band at 1025 cm^{-1} corresponds to the C–N^+ vibration of the piperidinium cationic in PTPiQA [43,44] which confirms the successful quaternization. However, we

acknowledge that the relatively low QGO loading hinders clear differentiation between the PTPiQA and PTPiQA–QGO-X membranes, as the characteristic vibrational signatures of QGO are largely masked by the dominant absorption bands of the polymer matrix.

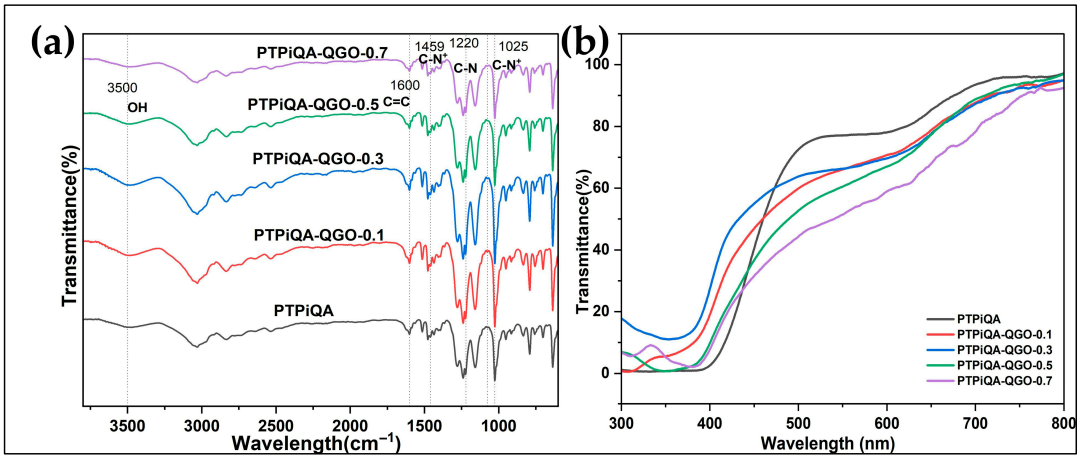


Figure 6. (**a**) FT-IR spectra of PTPiQA and PTPiQA-QGO-X membranes; (**b**) UV-vis spectra of PTPiQA and PTPiQA-QGO-X membranes.

3.3.2. UV Visible Spectroscopy

The UV–Visible transmission spectra of pristine PTPiQA and its composite membranes with varying QGO content (0.1–0.7 wt%) in Figure 6b reveal distinct optical behavior. PTPiQA exhibits the highest transmittance, whereas the introduction of QGO leads to a gradual reduction in transmission intensity, reflecting the combined effects of light absorption and scattering by the dispersed nanofiller. Two notable spectral regions can be distinguished in the 300–400 nm range, and all samples display a feature associated with a π-π^* transition of aromatic C=C bonds from the polyterphenylene backbone and the sp^2 carbon domains of QGO. It is observed that increasing QGO loading induces a broader decrease in transmittance, which can be linked to n-π^* transitions involving C=O groups within the QGO structure and additional optical scattering from the heterogeneous filler distribution. This attenuation becomes more pronounced at higher QGO contents, particularly for the 0.5 wt% and 0.7 wt% membranes, suggesting increased aggregation. These observations align with previous studies on the incorporation of GO in AEMs [6], where a similar reduction in the transmittance has been reported to be due to filler matrix interactions and increased optical scattering.

3.4. Morphology of PTPiQA and PTPiQA-QGO-X Membranes

The SEM surface morphology of PTPiQA membranes, reinforced with varying amounts of QGO, shows surface characteristics with increasing QGO content (Figure 7). Figure 7a shows that the PTPiQA membrane exhibits a smooth, homogeneous surface, indicating a well-formed polymer matrix without phase separation. When 0.1% QGO is incorporated, the membrane surface remains relatively smooth, with only slight irregularities, suggesting that the QGO is finely dispersed and well-integrated (Figure 7b). Even when the loading of the filler is increased to 0.3% the surface appears to remain homogeneous, indicating effective filler dispersion without aggregation (Figure 7c). As the QGO content increases to 0.5% there is a noticeable increase in surface roughness, likely due to the formation of localized ionic clusters, while maintaining good structural integrity (Figure 7d). However, at the highest QGO content of 0.7% in Figure 7e, significant agglomeration is observed, with clustered QGO particles disrupting the uniform surface, indicating poor dispersion and reduced compatibility, which could impair ion transport

and mechanical properties. Further, SEM cross-sectional images of PTPiQA membranes with varying QGO content reveal differences in internal morphology as a function of filler concentration (Figure 8a–e).

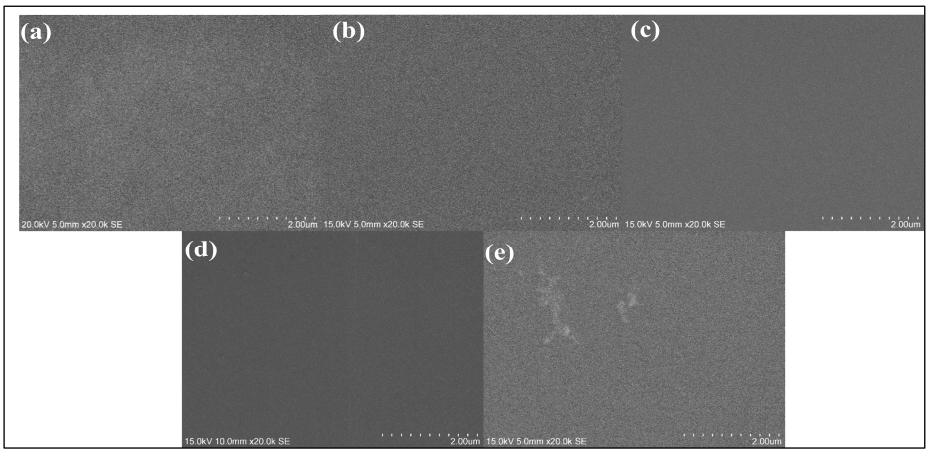


Figure 7. Surface SEM images of PTPiQA-based membranes with varying amounts of QGO filler: (**a**) PTPiQA, (**b**) PTPiQA-QGO-0.1%, (**c**) PTPiQA-QGO-0.3%, (**d**) PTPiQA-QGO-0.5%, and (**e**) PTPiQA-QGO-0.7%.

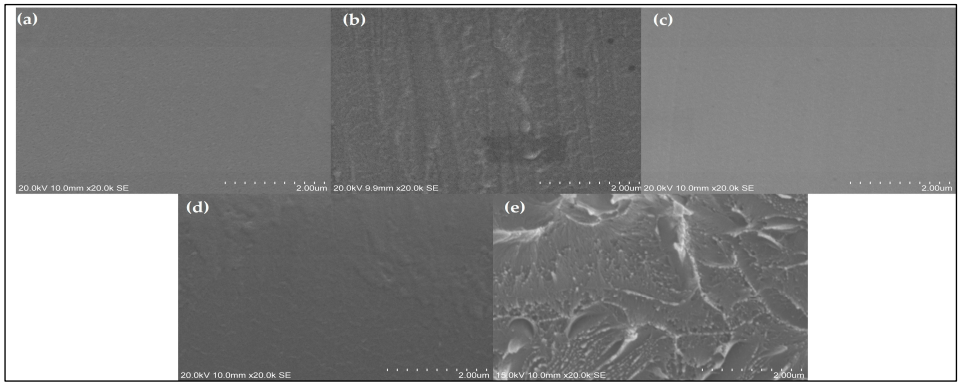


Figure 8. Cross-sectional FESEM images of PTPiQA-based membranes with varying QGO content: (**a**) PTPiQA, (**b**) PTPiQA-QGO-0.1%, (**c**) PTPiQA-QGO-0.3%, (**d**) PTPiQA-QGO-0.5%, and (**e**) PTPiQA-QGO-0.7%.

The neat membrane shows a compact, dense structure with no visible defects, indicating good polymer chain entanglement (Figure 8a). Membranes with 0.1% and 0.3% QGO appear to remain largely uniform, smooth, and compact, with only subtle textural changes reflecting minimal structural disturbance, suggesting that the QGO is well-dispersed within the matrix (Figure 8b,c). However, a slight roughness appears at 0.5% QGO, indicating the onset of ionic clustering while maintaining an overall coherent structure (Figure 8d). When the QGO (Figure 8e) content is increased to 0.7%, the cross-sectional morphology shows clear signs of agglomeration, with clustered and uneven regions indicating poor filler dispersion, which could compromise the mechanical robustness of the membrane and ion transport efficiency. The membrane thickness observed from cross-sectional SEM images ranged from approximately 57 µm to 145 µm.

Additionally, the surface roughness parameters evaluated from the AFM 3D images show average roughness (Sa), root mean square roughness (Sq), and peak to valley height (Sz), details of which are shown in Figure 9a–e and presented in Table 1 [45–48]. The neat PTPiQA membrane exhibits the highest roughness among all samples, with a Sa of 4.51 nm, an Sq of 5.38 nm, and an Sz of 20.8 nm. However, this is not due to poor surface morphology

of the membrane but is attributed to the curved surface of the membrane as seen from the 3D image (Figure 9a). Incorporation of 0.1 wt% QGO resulted in a dramatic decrease in roughness, as evidenced by a significant reduction in Sa, Sq, and Sz (Table 1). This suggests a considerable smoothing of the membrane surface, likely due to dispersion of QGO, resulting in planarization of the polymer matrix. While an increase in the QGO content to 0.3 wt% (Figure 9c) led to a slight rise in roughness relative to 0.1 wt% filler, a more marked increase in roughness occurred for 0.5 wt% QGO (Figure 9d). Interestingly, the average roughness and root mean square roughness for the membrane with 0.7 wt% QGO decreased (Figure 9e), while the peak to valley height increased, likely due to aggregation of QGO at higher loadings, leading to localized surface roughness.

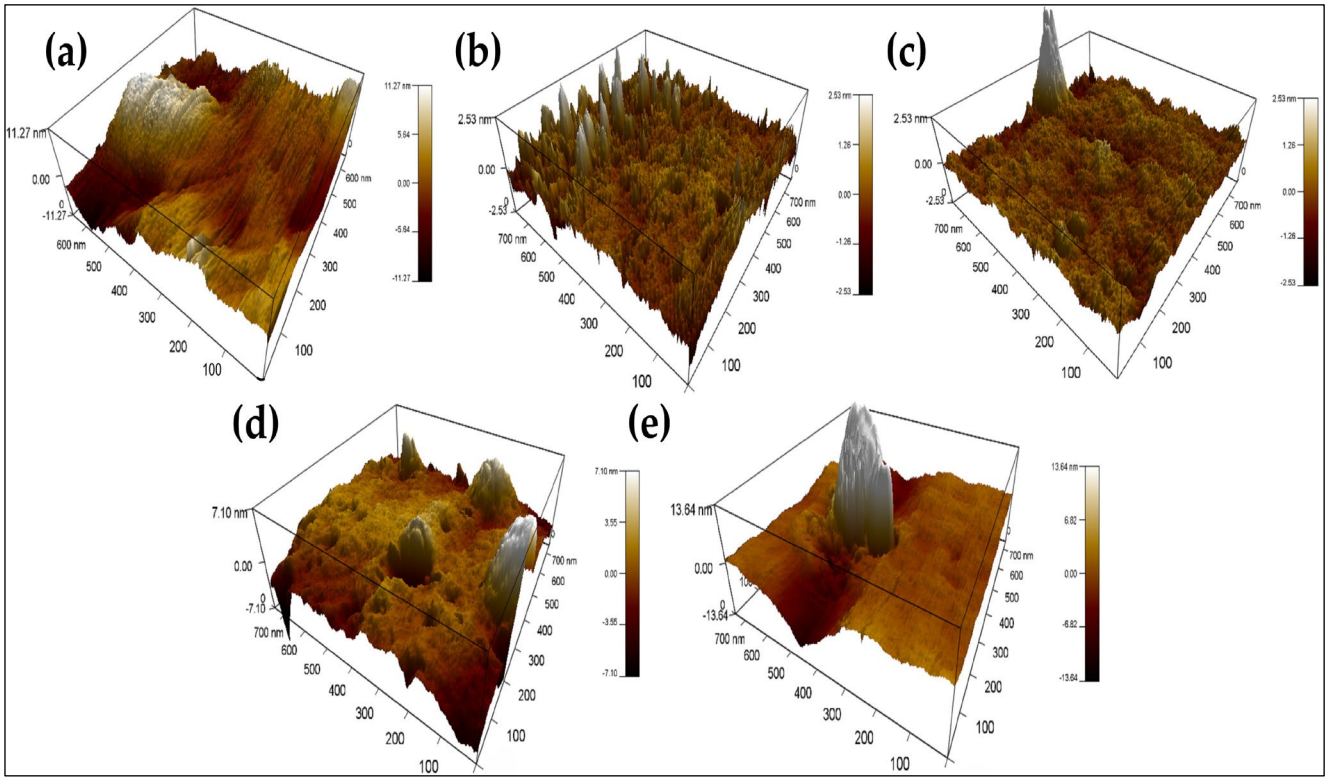


Figure 9. AFM 3D images of PTPiQA-based membranes with varying QGO content: (**a**) PTPiQA, (**b**) PTPiQA-QGO-0.1%, (**c**) PTPiQA-QGO-0.3%, (**d**) PTPiQA-QGO-0.5%, and (**e**) PTPiQA-QGO-0.7%.

Table 1. Surface roughness parameters of the membranes resulting from analysis of the AFM images.

Membrane	Sa (nm)	Sq (nm)	Sz (nm)
PTPiQA	4.51	5.38	20.80
PTPiQA-QGO-0.1%	0.24	0.30	2.12
PTPiQA-QGO-0.3%	0.28	0.41	2.41
PTPiQA-QGO-0.5%	0.57	0.92	3.28
PTPiQA-QGO-0.7%	0.52	0.67	4.07

3.5. Water Uptake and Swelling Ratio

Backbone stiffness and cation structure critically influence WU and SR, which determine the dimensional stability of the AEM. Rigid, contorted polymer backbones tend to suppress swelling even when WU is moderate. For instance, membranes with twisted, rigid, and contorted units have very low linear swelling (<8% at 20–80 °C) while still absorbing significant amounts of water [49]. Additionally, the nature of the QA and co-

monomer can be tuned to achieve phase-separated morphology, which helps to maintain WU and SR [50,51]. In this study, PTPiQA membranes show a systematic increase in the WU and SR with increasing loading of QGO, reflecting the influence of the hydrophilic filler and the inherent free volume in the PTPiQA backbone [52] (Table 2). Even though a twisted structure with substitution has been reported to control the SR [53], this study has shown that the addition of quaternized hydrophilic QGO filler enhances water uptake, possibly aided by free volume arising from the twisted backbone, as evidenced by the water uptake of 46.4% and SR of 19.2% for PTPiQA, both of which are lower than that for the composites PTPiQA-QGO-X (Figure 10a). For instance, incorporating 0.1% QGO results in a slight increase in the WU to 48.7% and the SR to 20.7%, indicating that the introduction of even a small amount of QGO enhances hydrophilicity without significantly perturbing the membrane structure, which is contrary to untwisted PPO-QGO [30]. As the QGO content is increased further between 0.3 and 0.7 wt%, the WU increases to 50.3–55.7% and the SR increases to 22.4–24.3%, which may be due to the formation of dispersed hydrophilic clusters that accommodate water efficiently without causing excessive swelling (Figure 10a).

Table 2. WU, SR, IEC, and OH^- conductivity at 20 °C for the PTPiQA membranes with varying QGO content.

Membrane	(WU) (%)	(SR) (%)	(IEC) (meq g^{-1})	OH^- Conductivity at 20 °C (mS cm^{-1})
PTPiQA	46.4 ± 4.77	19.2 ± 0.42	2.48 ± 0.11	17.28 ± 1.86
PTPiQA-QGO-0.1%	48.7 ± 4.37	20.7 ± 1.5	2.51 ± 0.18	22.49 ± 1.45
PTPiQA-QGO-0.3%	50.3 ± 3.73	22.4 ± 2.85	2.57 ± 0.09	71.56 ± 4.6
PTPiQA-QGO-0.5%	53.2 ± 4.62	23.1 ± 2.3	2.76 ± 0.19	13.29 ± 0.92
PTPiQA-QGO-0.7%	55.7 ± 3.03	24.3 ± 2.06	2.42 ± 0.1	13.63 ± 0.89

Note: All values are calculated at 20 °C.

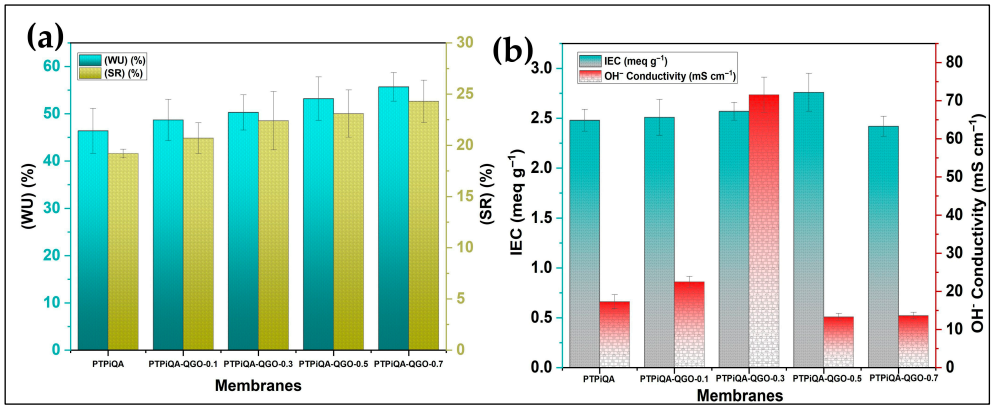


Figure 10. (**a**) Water uptake (WU) and swelling ratio (SR) of PTPiQA-based membranes with varying QGO content, (**b**) Ion exchange capacity (IEC, meq g^{-1}), and OH^- conductivity (mS cm^{-1}) of the membranes at varying QGO loadings (X = 0.1, 0.3, 0.5, and 0.7 wt%).

3.6. Ion Exchange Capacity

IEC represents the number of milli-equivalents (meq) of ion-exchangeable groups present per gram of membrane. In general, increasing IEC tends to raise OH^- conductivity, since more charge sites result in greater water uptake, which facilitates ion transport. However, this trend is not strictly linear, as excessive filler content can introduce ionic aggregation and disrupt ion pathways, which prevents the increase in IEC from translating into higher conductivity [52]. Interestingly, while the IEC of the membranes increased at moderate QGO loadings it decreased above 0.5 wt% filler, as shown in Table 2. The IEC

of 2.48 meq g^{-1} for PTPiQA is slightly lower than the theoretical value of 2.80 meq g^{-1} in OH^- form, which is presumably due to incomplete quaternization [21]. The increase to 2.51 meq g^{-1} with a QGO content of 0.1%, reflects the introduction of additional ionic sites from the QGO. The most significant improvement occurs for the composite with 0.5 wt% QGO as the IEC reaches 2.76 meq g^{-1} compared to QGO-0.3% which has an IEC of 2.57 meq g^{-1} (Figure 10b and Table 2), which is attributed to the contribution of QGO as the additional quaternary ammonium-rich domains increase the effective ion exchange capacity of the membrane. However, when the QGO content is increased to 0.7%, the IEC decreases to 2.42 meq g^{-1} due to agglomeration of QGO and non-homogeneous dispersion of QGO within the membrane [54].

3.7. Hydroxide Conductivity

The hydroxide conductivity of a membrane is strongly dependent on the type and loading of cationic functionality, the backbone architecture, and phase-separated morphology. More importantly, the conductivity of an AEM is highly temperature dependent [55,56], typically increasing 2–3 fold with increasing temperature from 20 to 30 °C to 80 °C due to reduced activation energy facilitated by better hydration and phase separation [39,52]. In addition, the conductivity can either be determined via in-plane measurement of ion movement along the membrane surface or through-plane measurement of ion transport across the membrane thickness [57–59]. In this study, the in-plane conductivity of PTPiQA and its QGO-filled composites was measured at room temperature in the OH^- form, the results of which are summarized in Table 2 and Figure 10b. The pristine PTPiQA membrane exhibited an in-plane conductivity of 17.28 mS cm^{-1} at 20 °C, which is comparable to the through-plane conductivity previously reported for the same membrane but with an IEC of 2.66 meq g^{-1} [39]. Upon incorporation of QGO, a noticeable enhancement in conductivity was observed, as the conductivity of PTPiQA–QGO-0.1 reached 22.49 mS cm^{-1}. This increase is attributed to the presence of the additional cationic groups introduced by QGO, with limited contribution to bulk transport. A maximum conductivity was achieved for composite PTPiQA–QGO-0.3, where the membrane exhibited a conductivity of 71.56 mS cm^{-1}, corresponding to a fourfold increase relative to pristine PTPiQA. This enhancement likely results from the combination of quaternized polymer and QGO filler, providing abundant ionic sites and hydration-induced directional pathways that facilitate efficient OH^- migration. Furthermore, the increased IEC (2.57 meq g^{-1}) and WU (50.3%) at this composition support the formation of well-connected and hydrated transport channels. Even though the IEC of QGO-0.1 and QGO-0.3 wt% are not significantly different, QGO-0.1 likely yields disconnected pockets of quaternary sites while QGO-0.3 fills the gaps and yields continuous channels. This is supported by the observation that composites with well-connected fillers have dramatically enhanced conductivities [27,60]. However, as the QGO content was increased to 0.5 wt% and 0.7 wt%, the conductivity decreased to 13.29 and 13.63 mS cm^{-1}, respectively, despite further increases in water uptake and comparable IEC values. This drop in performance is most likely due to the agglomeration of QGO impeding the ionic conduction network. Such a trend is consistent with QPPO-based AEMs [30], where conductivity improved up to an optimal QGO content but decreased at higher filler levels due to aggregation and increased tortuosity.

3.8. Mechanical and Thermal Stability

Mechanical characteristics, TS and EB, are essential indicators of the structural integrity of AEM. Consequently, the mechanical properties of neat PTPiQA and QGO-reinforced PTPiQA membranes were thoroughly examined under dry and wet conditions to simulate operational environments typical of AEMWEs and AEMFCs.

The mechanical properties of PTPiQA-based membranes were evaluated under both dry (45–60% RH) and wet conditions to assess their structural integrity and flexibility, the details of which are illustrated in Figures 11a and 11b, respectively. The neat PTPiQA membrane exhibited a dry tensile strength of 31.52 MPa and an elongation at break of 2.81%, indicating moderate strength and rigidity. Upon hydration, the TS decreased markedly to 13.56 MPa while the EB increased to 29.4%, reflecting the plasticizing effect of absorbed water, which enhances chain mobility but compromises mechanical strength. This behavior is consistent with the twisted terphenylene backbone, which introduces free volume to facilitate ion transport at the expense of mechanical rigidity, which is lower than previously reported values for terphenylene membranes [53]. Incorporation of 0.1 wt% QGO led to a slight increase in the dry TS to 34.70 MPa, while the EB remained nearly unchanged at 2.77%, suggesting effective stress transfer through well-dispersed QGO without severely restricting flexibility [61]. Under wet conditions, the TS increased to 16.91 MPa, indicating reinforcement under hydrated conditions; however, the EB decreased quite markedly to 16.52%, reflecting a trade-off between stiffness and ductility due to restricted segmental motion from the rigid filler.

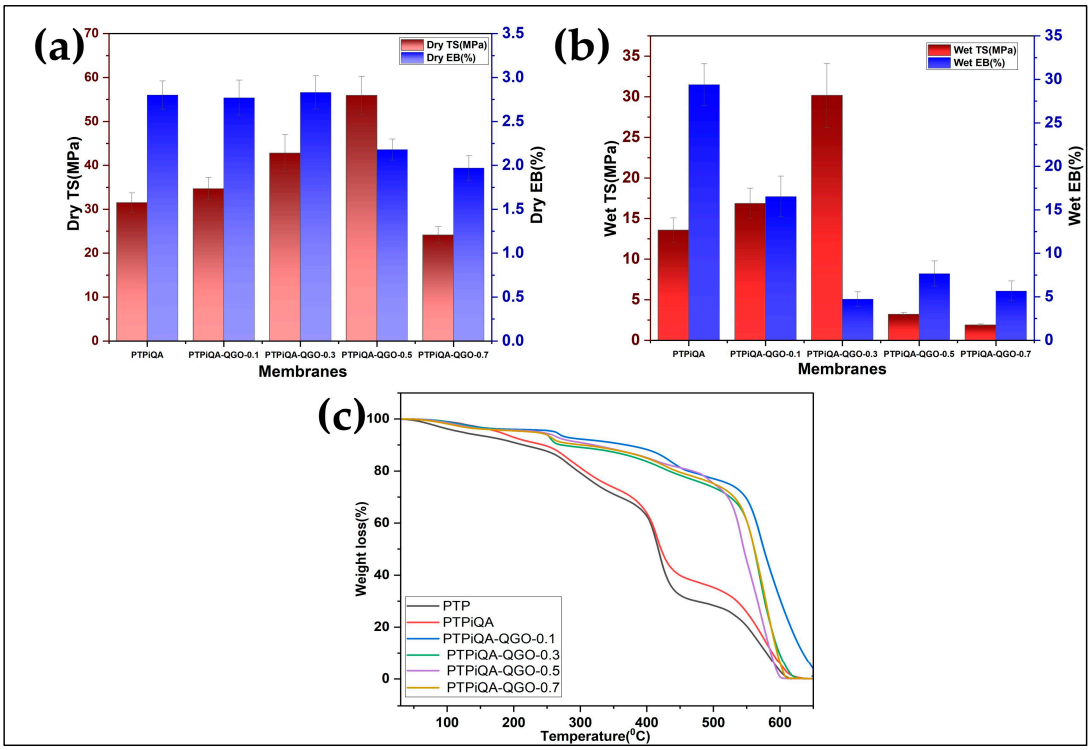


Figure 11. Tensile stress at break (TS) and elongation at break (EB) of PTPiQA membranes with varying QGO content under (**a**) dry and (**b**) wet conditions, and (**c**) TGA curves showing thermal stability of the membranes with different QGO loadings.

Composite with 0.3 wt% QGO exhibited a maximum dry TS of 42.77 MPa, which decreased to 30.20 MPa under wet conditions, confirming optimal filler dispersion and load transfer. However, this reinforcement came with reduced elongation as the dry EB remained at 2.83%, while EB of 4.73% under wet conditions was much lower than the 16.52% for the composite with 0.1 wt% QGO, indicating increased rigidity caused by a percolated filler network that limits chain extension under stress. In contrast, higher QGO loadings of 0.5 and 0.7 wt% resulted in deterioration of both dry and wet TS (55.9 and 3.22 MPa for 0.5 wt% QGO and 24.17 to 1.91 MPa for 0.7 wt% QGO, respectively), indicating poor filler dispersion and possible agglomeration, which can serve as stress concentrators to initiate

mechanical failure. The dry EB values dropped further to 2.18% and 1.97%, while the wet EB improved slightly to 7.68% and 5.67%, respectively, possibly due to local swelling-induced softening in water, but without effective reinforcement. These results clearly indicate that an optimal QGO content around 0.3 wt% is necessary to achieve a desirable balance between mechanical strength and flexibility in both dry and hydrated states.

The thermal stability of the membranes was also evaluated using TGA, comparing PTP and PTPiQA with QGO-reinforced composites (Figure 11c). The unmodified PTP precursor exhibited the lowest thermal stability among all samples, with the onset of decomposition at approximately 230 °C and rapid mass loss between 250 °C and 430 °C. There was an initial weight loss around 150 °C, followed by major degradation starting at approximately 200 °C, corresponding to the breakdown of the polymer backbone, with complete decomposition around 400 °C [39,52]. The quaternized polymer showed a similar TGA profile with only a marginal improvement in thermal stability. The incorporation of 0.1 wt% QGO resulted in a marked increase in the onset of degradation to 250 °C, with the final mass loss occurring close to 550 °C, reflecting enhanced thermal stability due to strong interfacial interactions between QGO and the polymer matrix. This delayed thermal decomposition is likely caused by the ability of the QGO filler to restrict polymer chain mobility and thereby enhance thermal resistance. Composites with 0.3–0.7 wt% QGO exhibited similar thermal stability profiles, but the onset of degradation started at slightly lower temperatures than for 0.1 wt% QGO. This slight decrease in thermal stability may be due to agglomeration of QGO within the matrix, diminishing the reinforcement effect and reducing thermal resistance. This observation aligns with the tendency of excessive filler loading to create localized stress points, thereby compromising the thermal integrity of the composite membrane. The TGA results indicated that all the fabricated membranes demonstrated good thermal stability up to 200 °C, highlighting their suitability as AEMs for fuel cell and electrolyser applications, which typically operate below this temperature [62].

3.9. Alkaline Stability

Alkaline stability is a critical parameter for evaluating the suitability of AEMs for electrolyser and fuel cell applications [63]. The limitations predominantly originate from the inherent nature and spatial arrangement of quaternized ammonium groups within the polymer matrix. Furthermore, the stability of the polymer backbone can be compromised due to degradation mechanisms such as β-hydrogen elimination (Hofmann or E2), nucleophilic substitution (S_N2), and ylide formation [64]. In PTPiQA systems, the piperidinium cation is vulnerable towards β-hydrogen elimination as well as S_N2 substitution of either the methyl or the cyclic methylene under harsh alkaline conditions. In this study, the alkaline stability of PTPiQA- and QGO-reinforced membranes was evaluated by immersing the membranes in 1 M KOH at 60 °C for 336 h and then drying at 60 °C for 6 h prior to analysis [65]. FTIR analysis of the membranes before and after alkaline stability testing revealed significant changes in characteristic peaks, indicating the extent of degradation and preservation of ionic functionalities (Figure 12a,b).

Prior to degradation, a broad OH-stretching vibration around 3500 cm^{-1} was observed, which increased in intensity with QGO content, reflecting enhanced hydrophilicity due to QGO hydroxyl groups. The spectrum also featured bands at 1600 cm^{-1} (aromatic C=C), 1459 cm^{-1} (quaternary C–N^+ stretching in QGO), 1220 cm^{-1} (C–N), and 1025 cm^{-1} due to the C–N^+ stretching of the piperidinium cation (Figure 12a). After 336 h, distinct spectral changes were observed. The OH band shifted slightly to 3398 cm^{-1}, with reduced intensity across all samples, indicating partial dehydroxylation or loss of adsorbed water. The aromatic C=C vibration also shifted slightly from 1600 cm^{-1} to 1579 cm^{-1}, suggesting minor conformational changes in the aromatic system. More importantly, a significant

reduction in the intensity of the C-N^+ stretching band at 1025 cm^{-1} as well as the band at 1220 cm^{-1} may well be indicative of partial degradation of QA groups. However, it is important to note that the degradation study from FT-IR spectroscopy does not give an exact degradation pathway.

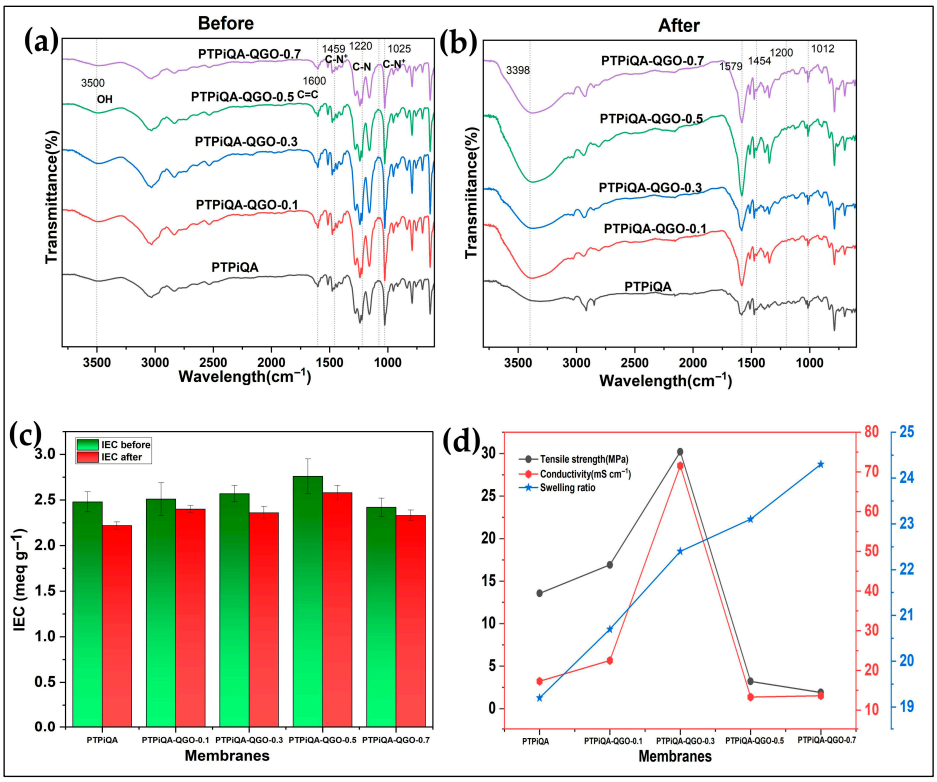


Figure 12. FTIR spectra of PTPiQA- and QGO-reinforced membranes (0.1 to 0.7 wt%) (**a**) before and (**b**) after alkaline stability testing in 1 M KOH at 60 °C for 336 h; (**c**) IEC of membranes before and after the alkaline stability test in 1 M KOH at 60 °C for 336 h; and (**d**) Multi parameter plot of conductivity and swelling ratio (**right** axis) and tensile strength (**left** axis) vs. QGO content.

Following the FT-IR analysis, alkaline stability was evaluated by monitoring changes in IEC after immersion in 1 M KOH at 60 °C for 336 h (Figure 12c) [65]. The neat PTPiQA membrane exhibited a reduction in IEC from 2.48 mmol g^{-1} to 2.22 mmol g^{-1}, corresponding to 89.5% retention of the piperidinium cations under alkaline stress, indicating moderate degradation. Upon incorporation of 0.1 wt% QGO, retention of IEC increased markedly to 95.6%, attributed to the initial barrier and shielding effects provided by the QGO nanosheets. At 0.3 wt% QGO, this retention decreased slightly to 91.8%, despite this membrane showing the highest hydroxide ion conductivity. This trend suggests that enhanced ionic connectivity and water uptake at this loading promote ion transport but also accelerate local hydroxide diffusion, leading to partial cation degradation. A further increase in the QGO content to 0.5 and 0.7 wt% improved IEC retention to 93.4% and 96.2%, respectively, indicating that the heterogeneous ionic pathway restricts access of hydroxide to the cationic sites. The multi-parameter plot (Figure 12d) shows that while composite with 0.3 wt% QGO maximizes TS (30.2 MPa) and conductivity (71.56 ± 4.6 mS cm^{-1}), the use of ≥0.5 wt% filler favors stability at the expense of conductivity and mechanical strength due to restricted hydroxide access and filler aggregation.

4. Conclusions

Composite AEMs PTPiQA–QGO-X were fabricated by impregnating poly(terphenylene piperi-dinium) with varying loadings of quaternized graphene oxide, and the influence of

QGO loading (0.1–0.7 wt%) on WU, SR, IEC, hydroxide conductivity, mechanical strength, and alkaline stability was systematically evaluated. Among all compositions, PTPiQA–QGO-0.3% delivered the best overall performance, achieving the highest in-plane hydroxide conductivity of 71.56 mS cm^{-1} at 20 °C, wet TS of 30.2 MPa with moderate SR (22.4%), and an IEC retention of 91.8% after heating at 60 °C in 1 M KOH for 336 h. Higher QGO loadings (0.5–0.7 wt%) enhanced alkaline stability (IEC retention up to 96.2%) due to filler-induced restriction of hydroxide access, but at the expense of conductivity and mechanical strength. These results demonstrate that, for PTPiQA, an optimal QGO content of 0.3 wt% provides a balance between ionic transport and mechanical robustness and demonstrates that QGO-reinforced PTPiQA membranes are potentially promising candidates for durable and high-performance AEMs in AEMWEs and AEMFCs.

Supplementary Materials: The following supporting information can be downloaded at: https://www.mdpi.com/article/10.3390/pr13103047/s1, Figure S1. N1s spectrum of (a) QGO and (b) PTPiQA; Table S1. Comparison table of this work with previously reported studies; Table S2. Weight and conductivity losses of PTPiQA and PTPiQA–QGO-0.7% membranes after alkaline stability testing (1 M KOH, 80 °C, 48h); Figure S2. Visual appearance of neat PTPiQA and PTPiQA–QGO-0.7% membranes before and after alkaline stability testing in 1 M KOH at 80 °C for 48 h, showing no obvious physical degradation, consistent with the low weight and conductivity losses measured; Figure S3. FTIR spectra of (a) neat PTPiQA and (b) PTPiQA–QGO-0.7% membranes before (black) and after (red) alkaline stability testing (1 M KOH, 80 °C, 48 h); Figure S4. Possible ionic channels of (a) before and (b) after hydration. References cited in Supplementary Materials [6,21,27,30,41,42,66,67].

Author Contributions: Conceptualization, T.P., M.M. and S.D.; methodology, T.P., M.M. and S.D.; software, T.P., H.A.E., M.M., S.D. and B.G.P.; validation, M.M., S.D., H.A.E. and B.G.P.; formal analysis, M.M., S.D., H.A.E. and B.G.P.; investigation, M.M., S.D. and B.G.P.; resources, H.A.E., M.M., S.D. and B.G.P.; data curation, T.P., M.M., S.D., H.A.E. and B.G.P.; writing—original draft preparation, T.P., H.A.E., M.M., S.D. and B.G.P.; writing—review and editing, T.P., M.M., S.D. and B.G.P.; visualization, T.P., H.A.E., M.M., S.D. and B.G.P.; supervision, M.M., S.D. and B.G.P.; project administration, M.M., S.D. and B.G.P.; funding acquisition, M.M. and B.G.P. All authors have read and agreed to the published version of the manuscript.

Funding: This research was funded by the Natural Sciences and Engineering Research Council of Canada (NSERC) Tier 1 Canada Research Chair in Clean Hydrogen Production funding reference number 00393501 and UKRI--EPSRC under grant reference EP/Y026098/1 for Global Hydrogen Production Technologies (HyPT) Center.

Data Availability Statement: The original contributions presented in this study are included in the article and in the Supplementary Materials. Further inquiries can be directed toward the corresponding author.

Acknowledgments: The researchers at the Clean Hydrogen Lab (UQTR, Institute for Hydrogen Research) would like to acknowledge the support of the Natural Sciences and Engineering Research Council of Canada (NSERC) Tier 1 Canada Research Chair in Clean Hydrogen Production. The researchers at the Clean Hydrogen Lab (CH2Lab, Hydrogen Research Institute—HRI, UQTR) would like to acknowledge the School of Engineering and the School of Natural and Environmental Sciences at Newcastle University for their valuable technical expertise and research support. The authors wish to acknowledge the support of UKRI-EPSRC under the Building a Green Future theme and the International Science Partnerships Fund as part of the Global Hydrogen Production Technologies (HyPT) Center and NSERC financial support for HyPT Center.

Conflicts of Interest: The authors declare no conflicts of interest.

References

1. Kober, T.; Schiffer, H.-W.; Densing, M.; Panos, E. Global Energy Perspectives to 2060—WEC's World Energy Scenarios 2019. *Energy Strategy Rev.* **2020**, *31*, 100523. [CrossRef]
2. Vujanović, M.; Wang, Q.; Mohsen, M.; Duić, N.; Yan, J. Recent Progress in Sustainable Energy-Efficient Technologies and Environmental Impacts on Energy Systems. *Appl. Energy* **2021**, *283*, 116280. [CrossRef]
3. Zou, C.; Li, S.; Xiong, B.; Liu, H.; Ma, F. Revolution and Significance of "Green Energy Transition" in the Context of New Quality Productive Forces: A Discussion on Theoretical Understanding of "Energy Triangle". *Pet. Explor. Dev.* **2024**, *51*, 1611–1627. [CrossRef]
4. Mondal, S.; Palit, D. Challenges in Natural Resource Management for Ecological Sustainability. In *Natural Resources Conservation and Advances for Sustainability*; Elsevier: Amsterdam, The Netherlands, 2022; pp. 29–59, ISBN 978-0-12-822976-7.
5. Adams, S.; Acheampong, A.O. Reducing Carbon Emissions: The Role of Renewable Energy and Democracy. *J. Clean. Prod.* **2019**, *240*, 118245. [CrossRef]
6. Ion-Ebrasu, D.; Pollet, B.G.; Caprarescu, S.; Chitu, A.; Trusca, R.; Niculescu, V.; Gabor, R.; Carcadea, E.; Varlam, M.; Vasile, B.S. Graphene Inclusion Effect on Anion-Exchange Membranes Properties for Alkaline Water Electrolyzers. *Int. J. Hydrogen Energy* **2020**, *45*, 17057–17066. [CrossRef]
7. Gupta, G.; Scott, K.; Mamlouk, M. Soluble Polystyrene-b-poly (Ethylene/Butylene)-b-polystyrene Based Ionomer for Anion Exchange Membrane Fuel Cells Operating at 70 °C. *Fuel Cells* **2018**, *18*, 137–147. [CrossRef]
8. Letchumanan, I.; Mohamad Yunus, R.; Mastar@Masdar, M.S.; Karim, N.A. Advancements in Electrocatalyst Architecture for Enhanced Oxygen Reduction Reaction in Anion Exchange Membrane Fuel Cells: A Comprehensive Review. *Int. J. Hydrogen Energy* **2025**, *104*, 527–546. [CrossRef]
9. Hossen, M.; Hasan, S.; Sardar, R.I.; Haider, J.B.; Mottakin; Tammeveski, K.; Atanassov, P. State-of-the-Art and Developmental Trends in Platinum Group Metal-Free Cathode Catalyst for Anion Exchange Membrane Fuel Cell (AEMFC). *Appl. Catal. B Environ.* **2023**, *325*, 121733. [CrossRef]
10. Vincent, I.; Kruger, A.; Bessarabov, D. Development of Efficient Membrane Electrode Assembly for Low Cost Hydrogen Production by Anion Exchange Membrane Electrolysis. *Int. J. Hydrogen Energy* **2017**, *42*, 10752–10761. [CrossRef]
11. Zakaria, Z.; Kamarudin, S.K. A Review of Alkaline Solid Polymer Membrane in the Application of AEM Electrolyzer: Materials and Characterization. *Int. J. Energy Res.* **2021**, *45*, 18337–18354. [CrossRef]
12. Willdorf-Cohen, S.; Zhegur-Khais, A.; Ponce-González, J.; Bsoul-Haj, S.; Varcoe, J.R.; Diesendruck, C.E.; Dekel, D.R. Alkaline Stability of Anion-Exchange Membranes. *ACS Appl. Energy Mater.* **2023**, *6*, 1085–1092. [CrossRef] [PubMed]
13. Meng, X.; Sun, C.; Mei, J.; Tang, X.; Hasanien, H.M.; Jiang, J.; Fan, F.; Song, K. Fuel Cell Life Prediction Considering the Recovery Phenomenon of Reversible Voltage Loss. *J. Power Sources* **2025**, *625*, 235634. [CrossRef]
14. Yan, S.; Yang, M.; Sun, C.; Xu, S. Liquid Water Characteristics in the Compressed Gradient Porosity Gas Diffusion Layer of Proton Exchange Membrane Fuel Cells Using the Lattice Boltzmann Method. *Energies* **2023**, *16*, 6010. [CrossRef]
15. Marino, M.G.; Kreuer, K.D. Alkaline Stability of Quaternary Ammonium Cations for Alkaline Fuel Cell Membranes and Ionic Liquids. *ChemSusChem* **2015**, *8*, 513–523. [CrossRef]
16. Wang, T.; Chen, D.; Wang, C.; Wei, H.; Ding, Y. Isomeric Poly(Arylene Piperidinium) Electrolyte Membranes with High Alkaline Durability. *Adv. Funct. Mater.* **2025**, *35*, 2422504. [CrossRef]
17. Palanivel, T.; Mamlouk, M.; Pollet, B.G.; Vinodh, R. Exploring Properties of Hyperbranched Polymers in Anion Exchange Membranes for Fuel Cells and Its Potential Integration for Water Electrolysis: A Review. *J. Energy Chem.* **2025**, *102*, 670–702. [CrossRef]
18. Jiang, T.; Wang, C.; Wang, T.; Wang, X.; Wang, X.; Li, X.; Ding, Y.; Wei, H. Imidazolium Structural Isomer Pyrazolium: A Better Alkali-Stable Anion Conductor for Anion Exchange Membranes. *J. Membr. Sci.* **2022**, *660*, 120843. [CrossRef]
19. Tan, X.; Sun, Z.; Pan, J.; Zhao, J.; Cao, H.; Zhu, H.; Yan, F. Alkaline Stable Pyrrolidinium-Type Main-Chain Polymer: The Synergetic Effect between Adjacent Cations. *J. Membr. Sci.* **2021**, *618*, 118689. [CrossRef]
20. Barnes, A.M.; Du, Y.; Zhang, W.; Seifert, S.; Buratto, S.K.; Coughlin, E.B. Phosphonium-Containing Block Copolymer Anion Exchange Membranes: Effect of Quaternization Level on Bulk and Surface Morphologies at Hydrated and Dehydrated States. *Macromolecules* **2019**, *52*, 6097–6106. [CrossRef]
21. Liu, F.H.; Yang, Q.; Gao, X.L.; Wu, H.Y.; Zhang, Q.G.; Zhu, A.M.; Liu, Q.L. Anion Exchange Membranes with Dense N-Spirocyclic Cations as Side-Chain. *J. Membr. Sci.* **2020**, *595*, 117560. [CrossRef]
22. Ponce-González, J.; Whelligan, D.K.; Wang, L.; Bance-Soualhi, R.; Wang, Y.; Peng, Y.; Peng, H.; Apperley, D.C.; Sarode, H.N.; Pandey, T.P.; et al. High Performance Aliphatic-Heterocyclic Benzyl-Quaternary Ammonium Radiation-Grafted Anion-Exchange Membranes. *Energy Environ. Sci.* **2016**, *9*, 3724–3735. [CrossRef]
23. Tarcan, R.; Todor-Boer, O.; Petrovai, I.; Leordean, C.; Astilean, S.; Botiz, I. Reduced Graphene Oxide Today. *J. Mater. Chem. C* **2020**, *8*, 1198–1224. [CrossRef]

24. Smith, A.T.; LaChance, A.M.; Zeng, S.; Liu, B.; Sun, L. Synthesis, Properties, and Applications of Graphene Oxide/Reduced Graphene Oxide and Their Nanocomposites. *Nano Mater. Sci.* **2019**, *1*, 31–47. [CrossRef]
25. Zhao, Y.; Fu, Y.; Hu, B.; Lü, C. Quaternized Graphene Oxide Modified Ionic Cross-Linked Sulfonated Polymer Electrolyte Composite Proton Exchange Membranes with Enhanced Properties. *Solid State Ion.* **2016**, *294*, 43–53. [CrossRef]
26. Zarrin, H.; Fu, J.; Jiang, G.; Yoo, S.; Lenos, J.; Fowler, M.; Chen, Z. Quaternized Graphene Oxide Nanocomposites as Fast Hydroxide Conductors. *ACS Nano* **2015**, *9*, 2028–2037. [CrossRef]
27. Das, G.; Park, B.J.; Kim, J.; Kang, D.; Yoon, H.H. Quaternized Cellulose and Graphene Oxide Crosslinked Polyphenylene Oxide Based Anion Exchange Membrane. *Sci. Rep.* **2019**, *9*, 9572. [CrossRef]
28. Manjula, N.; Balaji, R.; Ramya, K.; Rajalakshmi, N. Hydrogen Production by Electrochemical Methanol Reformation Using Alkaline Anion Exchange Membrane Based Cell. *Int. J. Hydrogen Energy* **2020**, *45*, 10304–10312. [CrossRef]
29. Zhang, D.; Xu, S.; Wan, R.; Yang, Y.; He, R. Functionalized Graphene Oxide Cross-Linked Poly(2,6-Dimethyl-1,4-Phenylene Oxide)-Based Anion Exchange Membranes with Superior Ionic Conductivity. *J. Power Sources* **2022**, *517*, 230720. [CrossRef]
30. Karakoti, M.; Im, K.S.; Jang, H.S.; Park, J.H.; Lee, D.J.; Kwon, H.W.; Nam, S.Y. Investigating the Impact of Functionalized Graphene Oxide on the Properties and Performance of Poly(2,6-Dimethyl-1,4-Phenylene Oxide)-Based Anion Exchange Membranes for Fuel Cells. *Electrochim. Acta* **2025**, *520*, 145868. [CrossRef]
31. Shin, D.W.; Guiver, M.D.; Lee, Y.M. Hydrocarbon-Based Polymer Electrolyte Membranes: Importance of Morphology on Ion Transport and Membrane Stability. *Chem. Rev.* **2017**, *117*, 4759–4805. [CrossRef] [PubMed]
32. Zhang, S.; Zhu, X.; Jin, C. Development of a High-Performance Anion Exchange Membrane Using Poly(Isatin Biphenylene) with Flexible Heterocyclic Quaternary Ammonium Cations for Alkaline Fuel Cells. *J. Mater. Chem. A* **2019**, *7*, 6883–6893. [CrossRef]
33. Du, X.; Zhang, H.; Yuan, Y.; Wang, Z. Constructing Micro-Phase Separation Structure to Improve the Performance of Anion-Exchange Membrane Based on Poly(Aryl Piperidinium) Cross-Linked Membranes. *J. Power Sources* **2021**, *487*, 229429. [CrossRef]
34. Gu, Y.; Dong, T.; Zhang, Y.; Li, Z.; Wang, Y.; Gao, J.; Lei, Y.; Wu, J.; Wang, Y.; Wang, Z. Microphase Separation Structures Facilitated by Dipole Molecules and Hydrogen Bonding in Poly (Biphenyl Piperidine-Isatin) Anion Exchange Membranes. *J. Power Sources* **2024**, *592*, 233918. [CrossRef]
35. Yue, X.B.; Liu, Y.J.; Lai, L.W.; Wang, X.H.; Peng, H.; Zhang, Q.G.; Zhu, A.M.; Liu, Q.L. Regulating the Microphase Separation Structure of Poly(Aryl-Alkylene) Anion Exchange Membranes through the Spatial Structure of the Main Chain. *Int. J. Hydrogen Energy* **2024**, *62*, 186–196. [CrossRef]
36. Ma, Y.; Hu, C.; Yi, G.; Jiang, Z.; Su, X.; Liu, Q.; Lee, J.Y.; Lee, S.Y.; Lee, Y.M.; Zhang, Q. Durable Multiblock Poly(Biphenyl Alkylene) Anion Exchange Membranes with Microphase Separation for Hydrogen Energy Conversion. *Angew. Chem. Int. Ed.* **2023**, *62*, e202311509. [CrossRef]
37. Yang, B.; Cunman, Z. Progress in Constructing High-Performance Anion Exchange Membrane: Molecular Design, Microphase Controllability and In-Device Property. *Chem. Eng. J.* **2023**, *457*, 141094. [CrossRef]
38. Xu, F.; Su, Y.; Lin, B. Progress of Alkaline Anion Exchange Membranes for Fuel Cells: The Effects of Micro-Phase Separation. *Front. Mater.* **2020**, *7*, 4. [CrossRef]
39. Wang, X.; Lin, C.; Gao, Y.; Lammertink, R.G.H. Anion Exchange Membranes with Twisted Poly(Terphenylene) Backbone: Effect of the N-Cyclic Cations. *J. Membr. Sci.* **2021**, *635*, 119525. [CrossRef]
40. Lee, A.Y.; Yang, K.; Anh, N.D.; Park, C.; Lee, S.M.; Lee, T.G.; Jeong, M.S. Raman Study of D* Band in Graphene Oxide and Its Correlation with Reduction. *Appl. Surf. Sci.* **2021**, *536*, 147990. [CrossRef]
41. He, H.; Chen, Q.; Fu, R.; Liu, Z.; Ge, L.; Xu, T. Side Chain Crosslinked Anion Exchange Membrane for Acid Concentration by Electrodialysis. *Chem. Bio. Eng.* **2024**, *1*, 647–657. [CrossRef]
42. Carboni, N.; Mazzapioda, L.; Caprì, A.; Gatto, I.; Carbone, A.; Baglio, V.; Navarra, M.A. Composite Anion Exchange Membranes Based on Graphene Oxide for Water Electrolyzer Applications. *Electrochim. Acta* **2024**, *486*, 144090. [CrossRef]
43. Wang, X.; Thomas, A.M.; Lammertink, R.G.H. Dimensionally Stable Anion Exchange Membranes Based on Macromolecular-Cross-Linked Poly(Arylene Piperidinium) for Water Electrolysis. *ACS Appl. Mater. Interfaces* **2024**, *16*, 2593–2605. [CrossRef]
44. Lee, J.H.; Yeon, J.S.; Kim, J.; Park, J.H.; Yoo, S.S.; Hong, S.; Kim, M.; Park, M.J.; Park, H.S.; Yoo, P.J. Accelerated Li-Ion Transport through a Zwitterion-Anchored Separator for High-Performance Li–S Batteries. *J. Mater. Chem. A* **2021**, *9*, 25463–25473. [CrossRef]
45. Hiesgen, R.; Morawietz, T.; Handl, M.; Corasaniti, M.; Friedrich, K.A. Atomic Force Microscopy on Cross Sections of Fuel Cell Membranes, Electrodes, and Membrane Electrode Assemblies. *Electrochim. Acta* **2015**, *162*, 86–99. [CrossRef]
46. Kardi, S.N.; Ibrahim, N.; Rashid, N.A.A.; Darzi, G.N. Investigating Effect of Proton-Exchange Membrane on New Air-Cathode Single-Chamber Microbial Fuel Cell Configuration for Bioenergy Recovery from Azorubine Dye Degradation. *Environ. Sci. Pollut. Res.* **2019**, *26*, 21201–21215. [CrossRef] [PubMed]
47. Gordano, A. AFM Analysis of Polymeric Membranes Fouling. *IgMin Res* **2024**, *2*, 399–405. [CrossRef]
48. Boussu, K.; Van Der Bruggen, B.; Volodin, A.; Snauwaert, J.; Van Haesendonck, C.; Vandecasteele, C. Roughness and Hydrophobicity Studies of Nanofiltration Membranes Using Different Modes of AFM. *J. Colloid Interface Sci.* **2005**, *286*, 632–638. [CrossRef] [PubMed]

49. Zhang, H.; Song, W.; Sun, L.; Yang, C.; Zhang, X.; Wu, M.; Wu, L.; Ge, X.; Xu, T. Anion Exchange Membrane with Pendulous Piperidinium on Twisted All-Carbon Backbone for Fuel Cell. *Membranes* **2024**, *14*, 121. [CrossRef]
50. Ozawa, Y.; Iwataki, T.; Uchida, M.; Kakinuma, K.; Miyatake, K. The Effect of the Piperidinium Structure on Anion-Exchange Membranes for Applications in Alkaline Water Electrolysis Cells. *J. Mater. Chem. A* **2023**, *11*, 19925–19935. [CrossRef]
51. Wu, X.; Chen, N.; Hu, C.; Klok, H.; Lee, Y.M.; Hu, X. Fluorinated Poly(Aryl Piperidinium) Membranes for Anion Exchange Membrane Fuel Cells. *Adv. Mater.* **2023**, *35*, 2210432. [CrossRef] [PubMed]
52. Mayadevi, T.S.; Sung, S.; Varghese, L.; Kim, T.-H. Poly(Meta/Para-Terphenylene-Methyl Piperidinium)-Based Anion Exchange Membranes: The Effect of Backbone Structure in AEMFC Application. *Membranes* **2020**, *10*, 329. [CrossRef] [PubMed]
53. Wang, X.; Lammertink, R.G.H. Dimensionally Stable Multication-Crosslinked Poly(Arylene Piperidinium) Membranes for Water Electrolysis. *J. Mater. Chem. A* **2022**, *10*, 8401–8412. [CrossRef]
54. Mothupi, M.L.; Msomi, P.F. Quaternized Polyethersulfone (QPES) Membrane with Imidazole Functionalized Graphene Oxide (ImGO) for Alkaline Anion Exchange Fuel Cell Application. *Sustainability* **2023**, *15*, 2209. [CrossRef]
55. Arunkumar, I.; Kim, A.R.; Lee, S.H.; Yoo, D.J. Enhanced Fumion Nanocomposite Membranes Embedded with Graphene Oxide as a Promising Anion Exchange Membrane for Fuel Cell Application. *Int. J. Hydrogen Energy* **2024**, *52*, 139–153. [CrossRef]
56. Xiao, Y.; Huang, W.; Xu, K.; Li, M.; Fan, M.; Wang, K. Preparation of Anion Exchange Membrane with Branch Polyethyleneimine as Main Skeleton Component. *Mater. Des.* **2018**, *160*, 698–707. [CrossRef]
57. Lim, J.H.; Hou, J.; Chun, J.; Lee, R.D.; Yun, J.; Jung, J.; Lee, C.H. Importance of Hydroxide Ion Conductivity Measurement for Alkaline Water Electrolysis Membranes. *Membranes* **2022**, *12*, 556. [CrossRef]
58. Ziv, N.; Dekel, D.R. A Practical Method for Measuring the True Hydroxide Conductivity of Anion Exchange Membranes. *Electrochem. Commun.* **2018**, *88*, 109–113. [CrossRef]
59. Zhao, Y.; Duan, L. Research on Measuring Pure Membrane Electrical Resistance under the Effects of Salinity Gradients and Diffusion Boundary Layer and Double Layer Resistances. *Membranes* **2022**, *12*, 816. [CrossRef]
60. Zhang, D.; Ye, N.; Chen, S.; Wan, R.; Yang, Y.; He, R. Enhancing Properties of Poly(2,6-Dimethyl-1,4-Phenylene Oxide)-Based Anion Exchange Membranes with 5-Mercaptotetrazole Modified Graphene Oxides. *Renew. Energy* **2020**, *160*, 250–260. [CrossRef]
61. Kahfi, A.; Kusumawati, N.; Setiarso, P.; Muslim, S.; Cahyani, S.A.; Zakiyah, N. Study in the Impact of Quaternized Graphene Oxide (QGO) Composition as Modifier on the Chemical, Physical, Mechanical, and Performance Properties of Polyvinylidene Fluoride (PVDF)-Based Nanocomposite Membrane. *CST* **2024**, *9*, 30–37. [CrossRef]
62. Yang, Y.; Li, P.; Zheng, X.; Sun, W.; Dou, S.X.; Ma, T.; Pan, H. Anion-Exchange Membrane Water Electrolyzers and Fuel Cells. *Chem. Soc. Rev.* **2022**, *51*, 9620–9693. [CrossRef] [PubMed]
63. Wu, Y.; Wu, C.; Varcoe, J.R.; Poynton, S.D.; Xu, T.; Fu, Y. Novel Silica/Poly(2,6-Dimethyl-1,4-Phenylene Oxide) Hybrid Anion-Exchange Membranes for Alkaline Fuel Cells: Effect of Silica Content and the Single Cell Performance. *J. Power Sources* **2010**, *195*, 3069–3076. [CrossRef]
64. Manohar, M.; Kim, D. Enhancement of Alkaline Conductivity and Chemical Stability of Quaternized Poly(2,6-Dimethyl-1,4-Phenylene Oxide) Alkaline Electrolyte Membrane by Mild Temperature Benzyl Bromination. *RSC Adv.* **2020**, *10*, 36704–36712. [CrossRef] [PubMed]
65. Kim, S.H.; Lee, K.H.; Chu, J.Y.; Kim, A.R.; Yoo, D.J. Enhanced Hydroxide Conductivity and Dimensional Stability with Blended Membranes Containing Hyperbranched PAES/Linear PPO as Anion Exchange Membranes. *Polymers* **2020**, *12*, 3011. [CrossRef]
66. Lee, K.H.; Chu, J.Y. Remarkable Conductivity and Durability of Anion Exchange Membrane with Poly(Fluorene-Terphenyl Piperidinium) Incorporating Graphene Oxide. *Int. J. Energy Res.* **2025**, *2025*, 4352185. [CrossRef]
67. Goel, P.; Mandal, P.; Bhuvanesh, E.; Shahi, V.K.; Chattopadhyay, S. Temperature Resistant Cross-Linked Brominated Poly Phenylene Oxide-Functionalized Graphene Oxide Nanocomposite Anion Exchange Membrane for Desalination. *Sep. Purif. Technol.* **2021**, *255*, 117730. [CrossRef]

Disclaimer/Publisher's Note: The statements, opinions and data contained in all publications are solely those of the individual author(s) and contributor(s) and not of MDPI and/or the editor(s). MDPI and/or the editor(s) disclaim responsibility for any injury to people or property resulting from any ideas, methods, instructions or products referred to in the content.